Biosensors and Bioelectronics 280 (2025) 117419

Contents lists available at ScienceDirect

Biosensors and Bioelectronics

journal homepage: www.elsevier.com/locate/bios

Rapid and sensitive biosensing of uropathogenic *E. coli* using plasmonic nanohole arrays on MIM: Bridging the gap between lab and clinical diagnostics

Hasan Kurt [a,*], Caner Soylukan [b,1], Süleyman Çelik [b,1], Eda Çapkın [b,c], Ibrahim Cagatay Acuner [d], Aynur Eren Topkaya [e], Meral Yüce [a,b,**]

[a] Department of Bioengineering, Imperial College London, South Kensington Campus, London, SW7 2AZ, UK
[b] SUNUM Nanotechnology Research and Application Centre, Sabanci University, Istanbul, 34956, Türkiye
[c] Faculty of Engineering and Natural Sciences, Sabanci University, 34956, Istanbul, Türkiye
[d] Department of Microbiology and Clinical Microbiology, Faculty of Medicine, Istinye University, 34010, Istanbul, Türkiye
[e] Department of Medical Microbiology, Faculty of Medicine, Yeditepe University, 34755, Istanbul, Türkiye

ARTICLE INFO

Keywords:
Metal-insulator-metal
Nanohole array
Uropathogenic *Escherichia coli*
Clinical diagnostics

ABSTRACT

This study introduces a novel biosensing platform, Plasmonic Array Nanohole Technology on Metal-Insulator-Metal (PANTOMIM), designed to overcome limitations of traditional plasmonic nanohole array biosensors. PANTOMIM utilizes a metal-insulator-metal structure as a lossy waveguide to dampen metal/substrate peaks, ensuring high extinction coefficients and spectral purity for biosensing. The architecture is optimized for the 800–850 nm wavelength range, with potential for future integration into nanophotonic devices. To demonstrate its clinical utility, we applied PANTOMIM to the detection of uropathogenic Escherichia coli (UPEC) in urine samples. This approach addresses the need for rapid diagnosis of urinary tract infections, providing results in 15 min and requiring minimal sample preparation. The efficacy of the technology was validated in a clinical setting with a cohort of 100 patients, showcasing its potential to revolutionize the detection of UPEC. PANTOMIM combines the advantages of plasmonic nanohole arrays, including tunable periodicity, coupled plasmonic response, and extraordinary optical transmission, while mitigating the challenges associated with thin-film plasmonic metals. This innovation paves the way for integrated nanoplasmonic biosensors for point-of-care diagnostics.

1. Introduction

Urinary tract infections (UTIs) are the most common bacterial infections in humans, reaching over 150 million incidences every year (Flores-Mireles et al., 2015). The prevalence of UTIs also result in considerably volume high clinical urine tests to determination of the culprit bacteria species. Standard clinical detection of UTIs predominanly relies on culture-based assays, which require 24–48 h for bacterial growth and subsequent identification of the bacteria species (Rowe and Juthani-Mehta, 2014). Culture-based methods are both labor-intensive and relatively slow procedures limiting the assay throughput, subsequent antibiotic susceptibility tests and timely administration of the correct antibiotic regiment. These issues of culture-based UTI assays also provide an unique opportunity for new detection methodologies such as refractometric plasmonic biosensors to demonstrate their efficacy and pave the way for their eventual commercialization in clinical setting.

Previous studies demonstrated proof-of-concept demonstration of Au crossed surface relief gratings and flow-through plasmonic nanohole arrays (Gomez-Cruz et al., 2018) for detection of prevalent cause of UTI, uropathogenic *E. coli* (Nair et al., 2018, 2020). Alternatively, plasmonic nanohole arrays were also utilized detection of sexually trasmitted infections such as *Neisseria gonorrhoeae* and *Chlamydia trachomatis* in urine (Cetin, 2024; Soler et al., 2017). However, these proof-of-concept

* Corresponding author. Department of Bioengineering, Imperial College London, South Kensington Campus, London, SW7 2AZ, UK.
** Corresponding author. SUNUM Nanotechnology Research and Application Centre, Sabanci University, Istanbul, 34956, Türkiye.
E-mail addresses: h.kurt@imperial.ac.uk (H. Kurt), meralyuce@sabanciuniv.edu (M. Yüce).
[1] Equal contribution.

https://doi.org/10.1016/j.bios.2025.117419
Received 3 February 2025; Received in revised form 11 March 2025; Accepted 24 March 2025
Available online 27 March 2025

plasmonic detection methodologies were not subjected to the rigorous clinical validation required to assess their performance in real-world settings. This gap highlights the need for additional research to bridge the transition from proof-of-concept demonstrations to clinically validated diagnostic tools.

Among these refractometric plasmonic biosensors, the plasmonic periodic nanohole arrays were frequently utilized for a number of reasons, but the leading reasons can be listed as the following.

i) The periodicity and nanohole diameter can be easily tuned to tailor the plasmonic response for desired spectral windows and refractometric sensitivity (Cetin et al., 2015).
ii) The coupled plasmonic response as the target analyte binds the detection surface unlike localized surface plasmon resonance (Yanik et al., 2010).
iii) They can provide extraordinary transmission (EOT) at resonance wavelengths (Yanik et al., 2011a).

However, the thin film nature of plasmonic metals used in EOT-type plasmonic biosensing can be identified as mixed blessing. One can excite surface plasmon polaritons (SPP) not only on the metal/medium interface but also on the metal-substrate interface, introducing an extra SPP resonance along with its higher modes (Kurt et al., 2021). They often can overlap with resonances of metal/medium SPPs and the substrate dielectric profile can be also coupled to the overall response of the metal/medium SPPs, resulting in hard-to-interpret spectral response (Cetin et al., 2015). A number of work-around solutions were proposed and implemented such as free-standing SiN membranes (Yanik et al., 2011b) limiting the substrate dielectric profile or using thick enough high refractive index (RI) SiN to red-shift the metal/substrate plasmon resonance or using thicker adhesion layer such as Ti to increase the imaginary component of the metal/substrate SPP (Belushkin et al., 2020; Li et al., 2017; Nair et al., 2020).

In this work, we proposed a modified architecture named "Plasmonic Array Nanohole Technology on Metal-Insulator-Metal" (PANTOMIM) to improve the abovementioned using metal-insulator-metal (MIM) structure and to pave the way for integrated nanoplasmonic biosensors. In particular, we utilized the MIM structure as a lossy waveguide to dampen the metal/substrate peaks to ensure high extinction coefficients while obtaining spectral purity for biosensing. Considering the commercialization route, we optimized the architecture for the wavelength range of 800–850 nm which can be viably detected using low-cost Si based sensors and can be further developed into integrated nanophotonic devices in the future. To showcase the technology, we aimed the detection of most prevalent UTI cause, uropathogenic *E. coli*, in urine. We developed a detection method using PANTOMIM UPEC biosensors to detect UPEC infections from urine within 15 min with minimal sample preparation severely reducing the diagnosis time. We validated our detection scheme in a clinical setting with a cohort of 100 patients.

2. Materials and methods

Please see supporting information for the details.

3. Results & discussion

3.1. Design, simulation, and nanofabrication of PANTOMIM sensors

We aimed to design a new class of plasmonic nanohole biosensors providing the following features:

i) High extinction coefficient at the resonance wavelength to facilitate robust detection using low-cost Si-based sensors.
ii) High spectral purity suppressing substrate effects to eliminate the spectral interference of metal-substrate plasmons with metal-medium plasmon polariton
iii) Open to further development into compact point of care devices

We were inspired by a layered architecture similar to the plasmonic super absorbers (Aydin et al., 2011) and pursued the metal-insulator-metal (MIM) architecture (Chanda et al., 2011) where high excinction coefficient can be achieved. We have selected square periodic nanohole geometry for polarization-independent response of the sensor. We utilized the MIM architecture as a lossy plasmonic waveguide to suppress the metal-substrate plasmon resonances. Instead of using EOT which provides ~1–2 % transmission for biosensing, we opted for reflection-based detection to increase the signal-to-noise ratio which would be compatible with the quantum efficiency profile of low-cost Si-based sensors.

The conceptual design of the PANTOMIM biosensor as shown in Fig. 1A, the architecture consisted of an Al thin film back reflector, an insulating dielectric layer (e.g. SiN, SiO_2), and a top Au metal layer with a square periodic nanohole array with a period of Λ and a diameter of hole of D. Al metal has a particularly high extinction coefficient in the wavelength range of 700–900 nm, providing a lossy back reflector inside the MIM waveguide (Lecarme et al., 2014). Meanwhile, the waveguide modes can be tuned with the thickness and RI of the dielectric layer. In finite-difference time-domain (FDTD) simulation of such architecture with a 100 nm Al back reflector, 75 nm SiN layer, 10 nm Ti adhesion layer and 100 nm thick Au nanohole array with a Λ of 550 nm and a D of 160 nm, we observed a significantly high electric field ($|E|$) enhancement of 23.6 ($|E|^2$ ~550) at resonance wavelength of ~800 nm in surrounding medium of water ($n = 1.33$). In Fig. 1A, we also observed a dipolar electric field enhancement in E_x component inside the nanohole and a dipole resonance at both the metal-medium interface and the metal-dielectric interface. As we investigate the electric field profiles in the xy-plane at slightly above (Z_1) and below (Z_2) the nanohole, the clear dipole resonances in the x and z components of the electric field were observed, as well as quadrupole resonance in E_y. When we probed inside the dielectric layer, we observed clear electric field propagation profiles in all 3 axes.

As we inquire into the effect of Λ in Fig. 1B, we observed a similar reflection profile to conventional nanohole arrays without the metal-substrate resonances and with strong Au/medium (1,0) and (1,1) modes. We only noticed a contribution of Au/SiN (1,0) substrate resonance for Λ lower than 500 nm. As we changed the thickness of the SiN layer, we observed the waveguide modes resembling the Fabry-Pérot (FP) modes as they are sandwiched between reflecting layers. In the case of the SiO_2 layer, we observed waveguide modes at higher thicknesses as SiO_2 has only an RI of 1.45 compared to the RI of SiN (~2.0). As these substrate-related modes can overlap with the metal-medium plasmon resonance, we kept the thickness of dielectric layer below 100 nm to ensure spectral purity. We also compared the optical density of reflectance spectra and the plasmon resonance quality factors of plasmonic nanohole arrays in FDTD simulations in Figs. S1 and S2. The plasmonic nanohole arrays with MIM architecture showed higher extinction at resonance wavelengths in comparison to plasmonic nanohole arrays on a transparent dielectric substrate (w/o MIM architecture). Similarly, plasmonic nanohole arrays with MIM architecture showed improved the quality factors (Q, $\omega_r/\Delta\omega$) of plasmon resonance mode of Au/medium (1,0). For Λ of 550 nm, plasmonic nanohole arrays with MIM architecture showed a quality factor of 40.67 while it showed only a quality factor of 21.99 in water medium ($n = 1.33$) (see Fig. S2).

We have also investigated the PANTOMIM architecture experimentally in comparison to FDTD simulations in Fig. 1C. We initially chose the Λ of 500, 550, and 600 nm for these fabrications. The spectral responses of PANTOMIM sensors show a high spectral match with the simulation results while showing a lower extinction coefficient in three

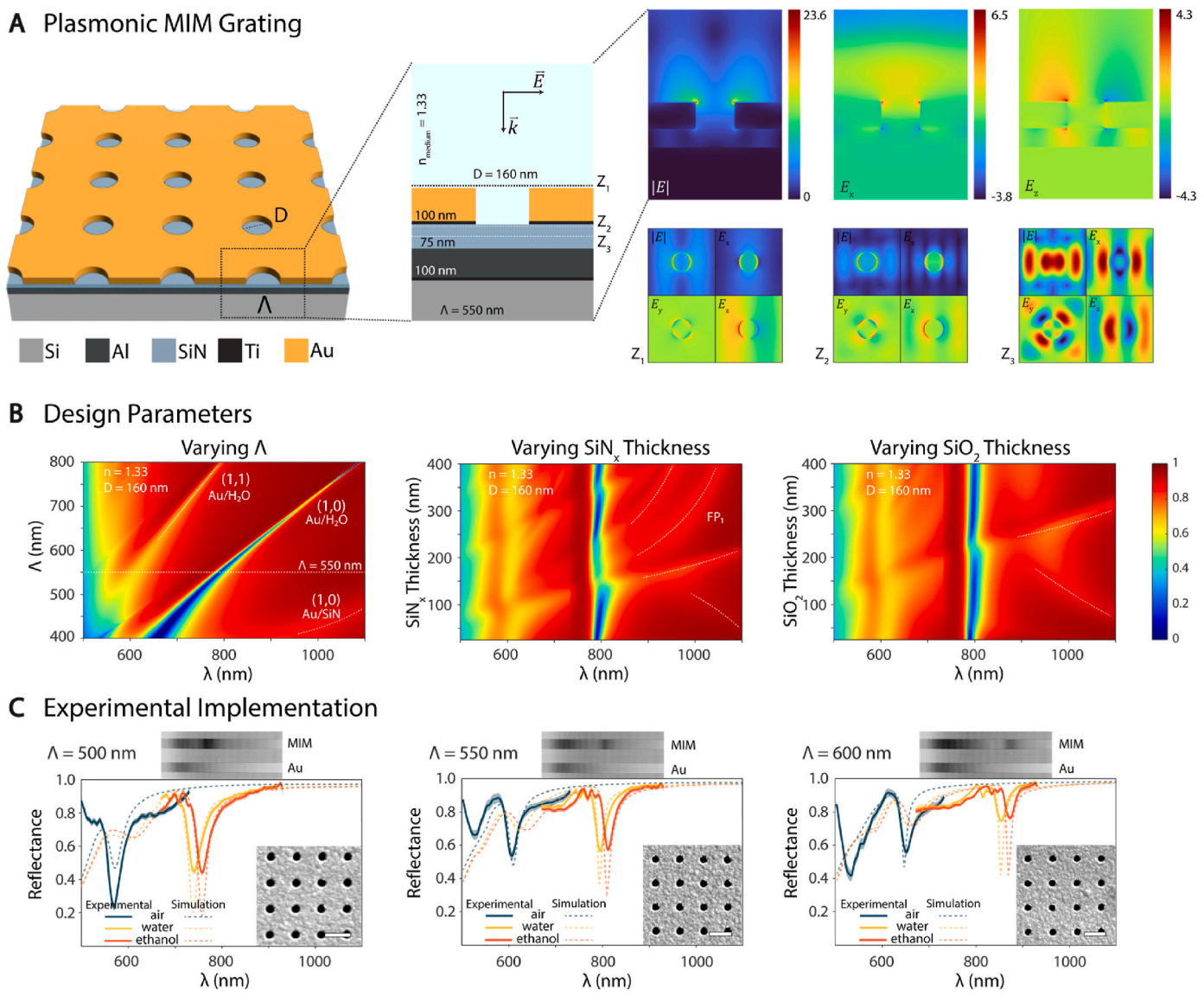

Fig. 1. **A** The architecture of plasmonic MIM nanohole arrays. The metal-insulator-metal stack consists of Al bottom metal layer, dielectric layer (e.g. SiN, SiO_2), patterned Au top metal layer with square-periodic (Λ) cylindrical perforations (diameter, D) and Ti adhesion layer. (left) The geometrical parameters for demonstrational electromagnetic simulation in a medium with an RI of 1.33 and the *p* polarized optical excitation in $-z$ direction (middle). The electric field distribution (magnitude of the electric field, $|E|$; *x* component of the electric field, E_x; *z* component of the electric field, E_z) in *xz* plane at the resonant wavelength of ~800 nm (upper). The electric field distribution (magnitude of the electric field, $|E|$; *x* component of the electric field, E_x; *z* component of the electric field, E_z) in *xz* plane at the resonant wavelength of ~800 nm (upper). The electric field distributions in *xy* planes where the monitor is at 1 nm above the top Au layer (Z_1), 1 nm below the Au-SiN interface (Z_2), and in the middle of the dielectric SiN layer (Z_3) at the resonant wavelength of ~800 nm (upper). The simulations were performed using the FDTD method. **B** The reflectance spectra of plasmonic MIM nanohole array with varying nanohole period from 400 to 800 nm (left), varying SiN layer (middle) or SiO_2 layer (right) thickness from 30 to 400 nm thickness, and nanohole diameter of 160 nm in surrounding medium of water ($n = 1.33$). The grating modes of Au/H_2O (1,0), Au/H_2O (1,1), Au/SiN (1,0), and the period of 550 nm are overlayed with white dashed lines (left). The Fabry-Pérot modes of the MIM structure are overlayed with white dashed lines. (middle and right) **C** The experimental and simulated reflectance spectra of plasmonic MIM nanohole arrays with periods of 500 nm (left), 550 nm (middle), and 600 nm (right) and hole diameter of 160 nm in air, water, and ethanol mediums. The solid lines designate experimental measurements. The dashed lines designate simulated responses. The SEM micrographs of each array were placed as inset into the reflectance spectra. The scale bars represent 500 nm. The spectral imaging response of plasmonic MIM nanohole arrays and flat Au thin films in ethanol were placed above the reflectance spectra of each array.

different mediums (air, water, and ethanol with RIs of 1.00, 1.3287, and 1.3573, respectively). In fact, surface roughness plays a critical role in the radiative losses of plasmonic nanostructures. As we increase the Λ, the difference in reflectance between experimental and simulated results widens. In line with our initial aimed features, we decided to continue with Λ of 550 nm as the resonance wavelength matches the extinction windows of the Al back reflector and quantum efficiency profile of Si-based sensors. Keeping in mind that increasing the Λ of nanohole arrays also increase the RI sensitivity of such sensors, we did not want to lose the high extinction coefficient and compatibility of Al extinction window and Si quantum efficiency profile as we aim to further develop such sensors as integrated plasmonic biosensors in the future.

For the nanofabrication of PANTOMIM sensors, we explored both etching and lift-off-based electron beam lithography (EBL) schemes, as shown in Fig. 2A. In both schemes, we used the same EBL resist, CSAR 6200.13, as it can provide respectable feature resolution in both routines. In both, we started with lightly p-doped polished Si (100) 4" wafers as substrates. The substrates were successively deposited with a 10 nm Ti adhesion layer and 100 nm Al back reflector layer. Later, we utilized plasma-enhance chemical vapor deposition (PECVD) for the

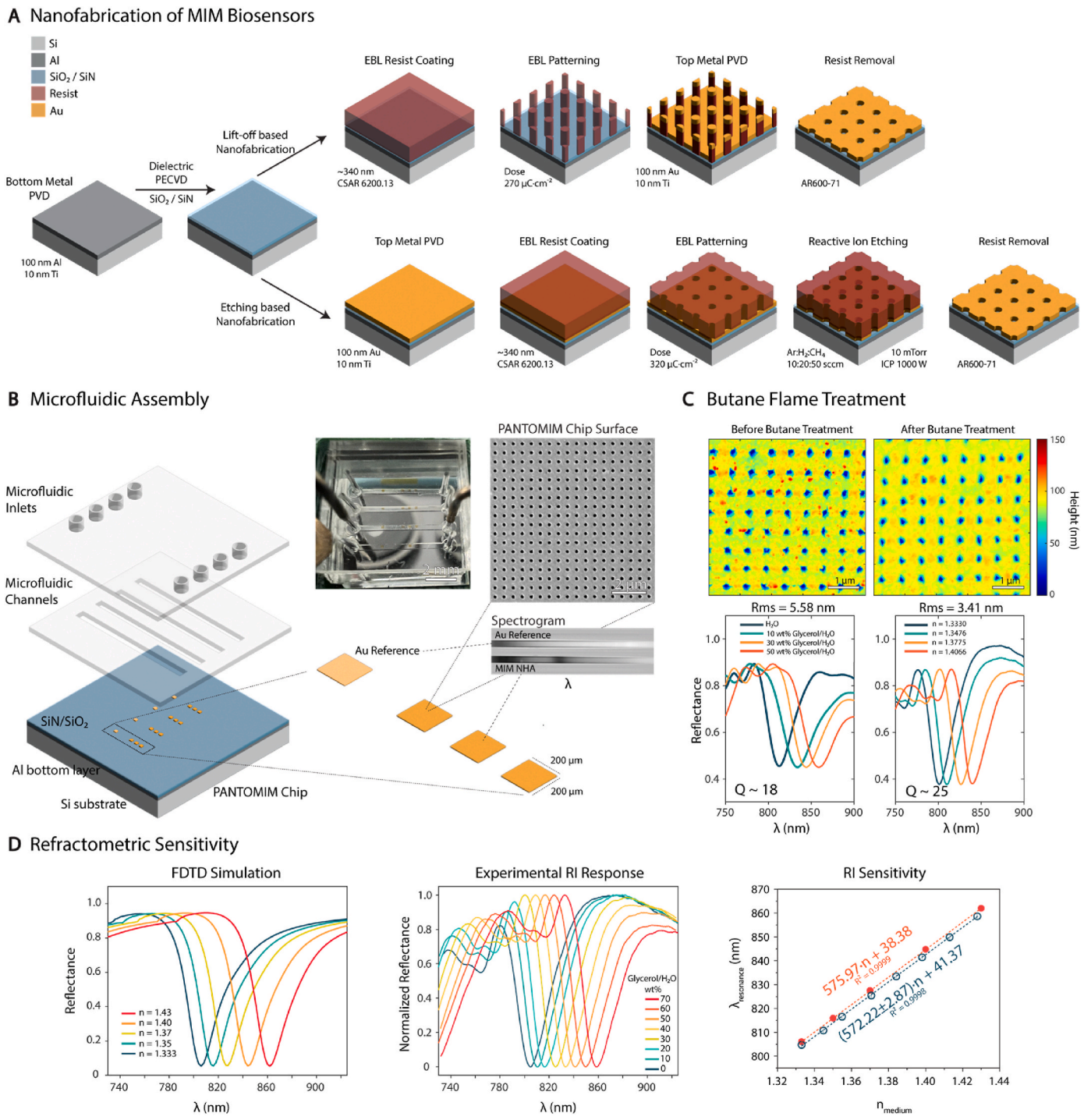

Fig. 2. **A** The nanofabrication process parameters for both lift-off and etching based routes. **B** The schematic representation of microfluidic assembly and on-chip plasmonic MIM nanohole array placement for 200 × 200 μm sensing sites. The assembled plasmonic MIM nanohole array chip is represented in the photograph where the scale bar represents 2 mm. The SEM micrograph shows the top surface of the plasmonic MIM nanohole array. The scale bar represents 2 μm. The image spectrogram of both flat Au reference and plasmonic MIM NHA. **C** The effect of butane flame treatment on plasmonic MIM NHA reading sites on their surface roughness. AFM height profile of both before and after butane treatment. The scale bars represent 1 μm. The root-mean-square (RMS) roughness was calculated as a whole image excluding the nanoholes. (top) The reflectance spectra of plasmonic MIM NHA reading sites were recorded before and after the butane flame treatment. The reflectance spectra were measured in different mediums with RI ranging from 1.333 to 1.4066. **D** The refractometric sensitivity of plasmonic MIM NHA reading sites was demonstrated in FDTD simulations (left) between RI ranging from 1.333 to 1.43 in different experimental glycerol/water mixtures (middle). The simulated and experimental plasmonic resonance peak shift versus the RI of the medium were represented along with calculated RI sensitivity in linear regression (right). The error bar of each individual point represents $\pm\sigma$ for $n = 5$.

deposition of SiN/SiO_2. We only tweaked the EBL dose for different nanofabrication schemes. Both nanofabrication routes have advantages over each other. Both methods provide high precision in the nanohole period. However, lift-off provides better control over the nanohole diameter. Etching-based nanofabrication provides smaller holes than the deployed EBL pattern. It can also vary depending on the dielectric layer. For 200 nm nanohole diameter in deployed EBL pattern, we obtained 160 nm nanohole diameter on SiN layers whereas 120 nm nanohole diameter on SiO_2 layers. In trade-off, etching-based nanofabrication provides more spherical nanoholes than the lift-off-based method. In terms of surface roughness, etching-based nanofabrication suffers from highly energetic etching conditions of Au and cannot provide a smoother surface, as shown in Fig. 1C.

3.2. Microfluidic assembly and bulk refractive index sensitivity of PANTOMIM sensors

For the microfluidic design of PANTOMIM sensors, we utilized 4 linear-channel geometry as shown in Fig. 2B. The microfluidic channels had a width of 200 μm, a height of 100 μm, and an inter-channel separation of 1 mm. For prototyping purposes, we used PDMS-based microfluidic channels, as they provide easier binding to SiN and SiO2 substrates. Each channel consists of one Au reference square pad and three replicas of PANTOMIM sensor square pads with a dimension of 200 μm. We utilized bent-metal fittings for liquid inlets and outlets to accommodate the working distance of our microscope objectives.

To remedy the radiative losses from surface roughness, we treated our PANTOMIM sensors with a brief butane-flame treatment of 20 s duration. The butane flame provides significantly enough temperature to melt the upper surface of Au layers, and later, the Au layer recrystallizes into a smoother and low-energy configuration. We quantified the level of improvement using atomic force microscopy in Fig. 2C. Root-mean-square (RMS) roughness of Au top layer was 5.58 nm prior, later reduced to 3.41 after butane flame treatment. Also, we checked the reflectance profiles of the same PANTOMIM sensors before and after butane flame treatment in 0, 10, 30, and 50 wt% glycerol/water solutions. The full-width half-maximum (FWHM) and the extinction of the primary resonance peaks were evidently improved. The quality factor of the Au/medium (1,0) plasmon resonance increased from Q ~ 18 to Q~ 25 as we apply butane treatment.

Finally, we used PANTOMIM sensors for their refractometric sensitivity using 0–70 wt% glycerol/water solutions after the above-mentioned modification. We also utilized FDTD simulations to track the RI sensitivity in parallel. The experimental and simulated RI sensitivity were investigated in biosensing relevant RI range of 1.3287–1.43. The linear regression of the simulated SPP red-shift response resulted in an equation of $575.97 \bullet n + 38.38$ with R^2 of 0.9999. Similarly, the linear regression of experimental SPP red-shift response was found as $(572.22 \pm 2.87) \bullet n + 41.37$ with R^2 of 0.9998. The simulated and experimental results were in accordance with each other.

3.3. Optical reader and liquid handling of PANTOMIM sensor

We employed several in-house microspectroscopy setups for the optical reading of the PANTOMIM sensors. Since the PANTOMIM relies upon grating-based momentum matching, the response of the plasmonic sensor depends on the polarization and incident angle of the incoming light. The polarization dependence can be eliminated using square periodicity by design. However, the plane-wave illumination of the plasmonic sensor still has to be provided. To ensure uniform plane-wave illumination of the sensor, we used a fiber-coupled tungsten halogen lamp, collimated the output using an aspheric lens and field iris, and later expanded the output using Keplerian beam expander consisting of an achromatic pair and iris. Later, we focused the collimated beam using an achromatic lens to the back focal plane of a low NA microscope objective to provide plane-wave illumination. This method suffers from the fact that only a fraction of the light can be collimated, as we used two irises. In later iterations, we used a parabolic reflector collimator to increase the collimation efficiency and decrease the setup size. As the microscope objectives, we utilized low NA low magnification apochromatic objective lenses since we aimed to analyze multiple PANTOMIM sensor pads simultaneously with minimal chromatic aberrations.

For the imaging and spectroscopy arms of the setups, we used dedicated arms with separate imaging lenses, as shown in Fig. 3A. For the imaging arm, we utilized an achromatic lens with a focal length of 200 nm and a CMOS camera. For the spectroscopy arm, we used an apochromatic tube lens to form an image on the slit plane of an imaging spectrometer equipped with a cooled EMCCD camera. Although the plasmonic resonances can be easily detected with a low-cost CMOS sensor as they have prominently high extinctions, we aimed to check for weak Fabry-Pérot and Au/substrate modes. In a later iteration, we combined the spectroscopy and imaging arm using a single apochromatic tube lens and a beamsplitter just before the CMOS imaging camera and imaging spectrometer. This way, we significantly reduced the size of the microspectroscopy setup and the size reduction from the reflector collimator addition. We also implemented a miniaturized custom-made lens-grating-lens type imaging spectrometer with a high-efficiency transmission grating and a low-cost CMOS sensor for the wavelength range of 780–850 nm. The prominent reflection dip can be easily tracked even with a low-cost CMOS sensor without any additional gain adjustment on the CMOS sensor.

For the liquid handling, we utilized a pressure-based flow control system with an electronically controlled 12-channel bidirectional distribution valve for the seamless sequential injection of samples in our main setup. In addition, we utilized a flow meter to ensure the flow rate and a bubble trap to eliminate any air ingress into the PANTOMIM sensors. Similar to the microspectroscopy setup, we also implemented a low-cost, miniaturized liquid handling system using piezoelectric double diaphragm micropumps with miniature valves and flow sensors.

Although we used the main microspectroscopy setup and pressure-based flow control systems exclusively for the following biosensing experiments, we wanted to show that these setups can be miniaturized and primed for commercial implementations.

3.4. Biofunctionalization of PANTOMIM sensors and biosensing performance

To transform our PANTOMIM refractometric sensors into biosensors, we first used the self-assembled monolayer method to chemically modify the surface to have chemically reactive moieties. We utilized a mixture of MUA/MUDA to completely functionalize the surface. As their alkane-based backbones of this molecules have high tendency to form close-packed monolayers and their mercapto-functionalized ends have pseudo-covalent interaction with metal surfaces, they can provide a well-defined functionalized monolayer on the surface of PANTOMIM sensor surface. In fact, the monolayer formation can be confirmed through the red-shift of the resonance wavelength, as shown in Fig. 4A.

In parallel, we investigated several polyclonal antibody targets and biofunctionalization routes for our ultimate target uropathogenic UPEC. First, we evaluated two widely accepted antibody immobilization schemes, proteinA-based affinity immobilization, and EDC-NHS covalent immobilization, using conventional SPR. We observed that proteinA-based affinity immobilization only manages to immobilize a limited amount of antibodies in question. Among them, antibody Ab137967 showed a 3-fold higher binding than other antibodies, Ab31499 and Bio-Rad. For covalent immobilization, we observed significantly higher binding across all antibodies, as shown in Fig. 4B. Thus, we opted for the AB137967 antibody for further sensor development. The immobilization routine was also validated with a commercial Quartz Crystal Microbalance (QCM) (Fig. S9). Since the covalent immobilization method is not affected by the orientation affinity binding like protein A, it can provide significantly higher coverage of the

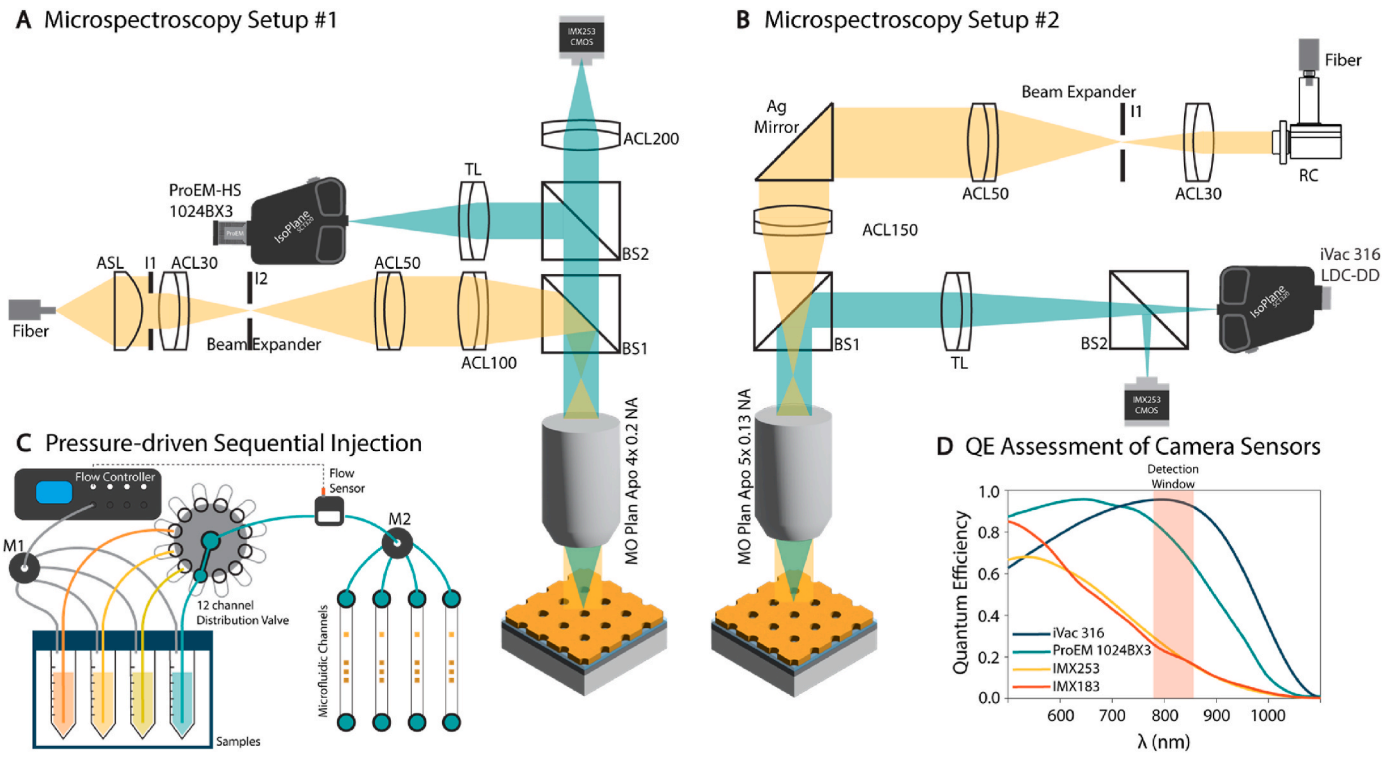

Fig. 3. **A** Design schematic of microspectroscopy setups #1. The in-house microspectroscopy setup uses a fiber-coupled broadband tungsten-halogen light source, and the illumination beam was collimated and expanded with an achromatic lens pair. The resulting illumination focused on the back focal plane of the microscope objective to planar illumination of the sample. The spectral and spatial imaging was obtained using 2 beamsplitters and separate lenses for each arm. **B** Design schematic of microspectroscopy setups #2. The illumination was collimated with a parabolic reflective collimator from the same light source. The beam was expanded using an achromatic lens pair, directed toward the main beamsplitter using a right-angle Ag mirror, and focused on the back focal plane of the microscope objective for plane illumination. The spectral and spatial detection was utilized in the same arm with an apochromatic tube lens and split into a spectrometer and imaging camera with an additional beamsplitter. **C** The pressure-driven sequential injection system. **D** Quantum efficiency assessment of camera-based sensors for development.

sensor surface. Since our target analyte is considerably large bacteria, we opted for a larger surface coverage of the covalent immobilization method (Kaymaz et al., 2023; Yüce and Kurt, 2017). The bacteria binding on the surface is often governed by the local avidity of the surface; higher coverage facilitates a more sensitive detection(Müller et al., 1998; Steen Redeker et al., 2013). In immobilization experiments of the PANTOMIM sensor, we observed a significant red shift after covalent immobilization of the selected antibody, AB137967, then a smaller shift upon the ethanolamine-based site blocking step, as shown in Fig. 4A.

To evaluate the biosensing performance of the PANTOMIM UPEC biosensor, we used gram-negative O4:K6 serotype uropathogenic bacterium *E. coli* strain J96 as the target analyte. In Fig. 4C, we also visualized the scale of *E. coli* and PANTOMIM biosensor surface in SEM micrograph. The bacterium has a 1–3 μm long rod shape with ~0.5 μm width and interacts with the plasmonic surface in both area and volume, resulting in a significant resonance redshift at higher concentrations, facilitating a sensitive biodetection. In Fig. 4D, we first evaluated the statistics of the blank sample (w/o UPEC) as it defines the absolute limit of detection of the PANTOMIM biosensor. We used a number of different PANTOMIM biosensors and different channels to evaluate the blank response. The PANTOMIM biosensor showed a mean (μ) response of $\sim 1.47 \times 10^{-14}$ nm resonance shift ($\Delta\lambda$) and a standard deviation (σ) of 0.13 nm, which is close to the resolution limit of our detection system (for 150 l/mm grating). For the biosensor characteristics of the PANTOMIM UPEC biosensor, we utilized Hill-Langmuir isotherm since this isotherm can take into account the relative reducing binding at neighboring sites as a large ligand is bound the surface as the following

$$\theta = \frac{[L]^n}{K^n + [L]^n} \tag{1}$$

where θ is the fraction of the surface coverage, K is the apparent dissociation constant, $[L]$ is the ligand concentration, and finally n is the Hill coefficient. The equation can be further modified for normalized response for a specific concentration of ligand C as the following.

$$\text{Response}(C) = \frac{1}{1 + 10^{n\,(\log K - \log C)}} \tag{2}$$

Then, the limit of detection for the biosensor can be obtained using standard deviation (σ) of blank measurements at $C = 0$.

$$LoD = \log K\left(10^{\frac{3\sigma}{n}} - 1\right) \tag{3}$$

To determine the biosensor characteristics of the PANTOMIM UPEC biosensor, we tracked the resonance shift ($\Delta\lambda$) for logarithmic UPEC concentration range of 1–10^6 cfu mL^{-1}. The Hill-Langmuir isotherm fit resulted in K value of 24.85 ± 4.09, n value of 0.264 ± 0.013 with R^2 of 0.99938. As we plug in the σ of the blank response of the PANTOMIM UPEC biosensor, we reached a limit of detection of 1.23 cfu mL^{-1} and a limit of quantification of 2.06 cfu mL^{-1}. We called it the absolute limit of detection as it disregards the non-specific interferants like other pathogenic bacteria in urinary track infections.

To assess the specificity and selectivity of the system, we also evaluated the binding characteristics of *E. coli* K12 (ATCC-PTA-7555), *S. aureus* (ATCC-15305), *C. freundii* (ATCC-8090), and *P. mirabilis* (ATCC-51286) at logarithmic concentration range of 1–10^6 cfu mL^{-1} (Fig. 4D). *E. coli* K12 is a low-virulence strain of *E. coli* that typically

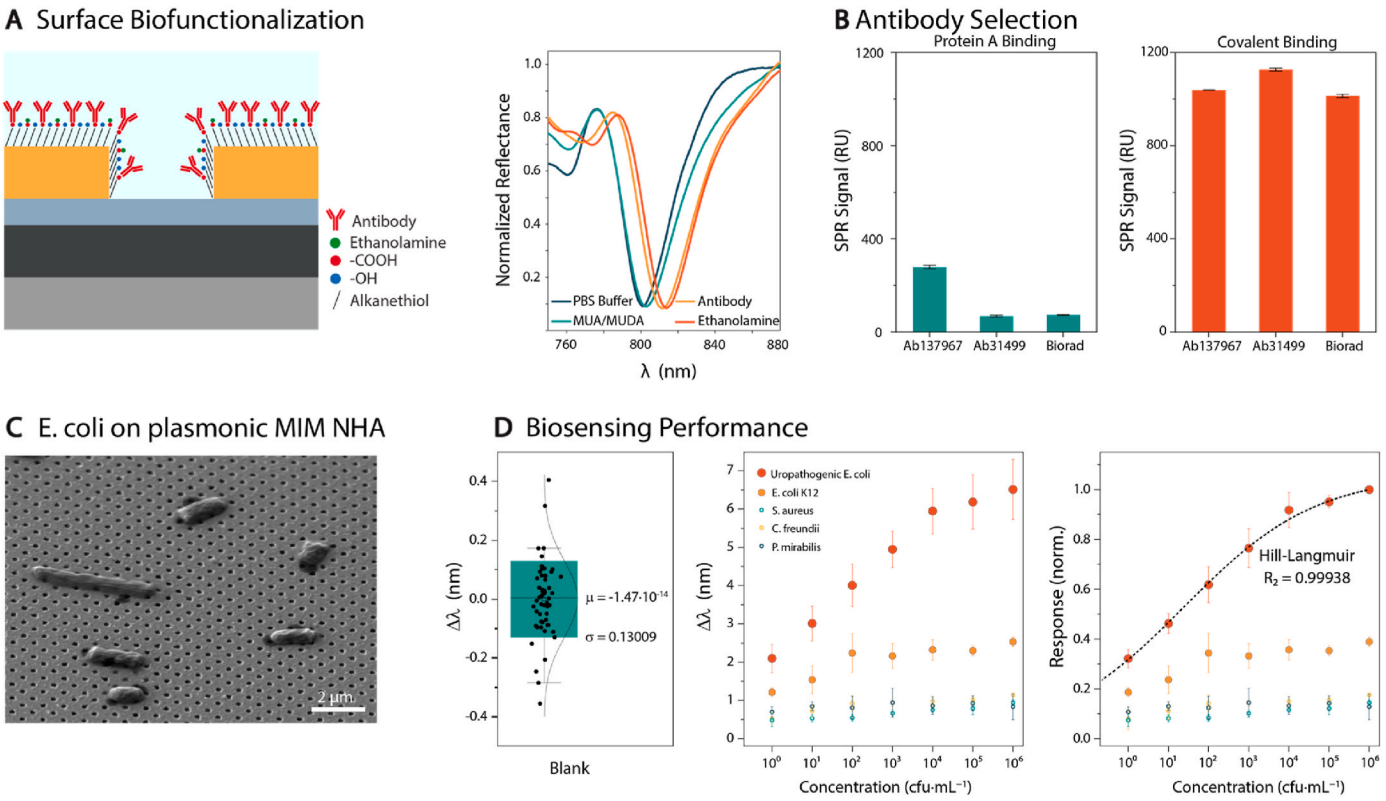

Fig. 4. **A** Surface biofunctionalization of plasmonic MIM NHA biosensors. (left) Normalized reflectance spectra after each immobilization step **B** Antibody and immobilization route selection. Error bars respesents $\pm\sigma$. The three replicates (n = 3) were analyzed in separate SPR channels. **C** SEM micrograph of uropathogenic *E. coli* on plasmonic MIM NHA biosensors. **D** Biosensing performance of plasmonic MIM NHA biosensors. The blank response statistics of the biosensor (left). The box chart range repesents $\pm\sigma$. The whiskers represent 5 and 95 percentile. The normal distribution is presented on the right of the box chart. The plasmon resonance wavelength dip change is presented for the selection of pathogens (Uropathogenic *E. coli*, *E. coli* K12, *S. aureus*, *C. freundii*, and *P. mirabilis*) within the logarithmic concentration range of 1–10^6 cfu mL^{-1} (middle) Normalized biosensor response for selected pathogens and fitted Hill-Langmuir curve for uropathogenic *E. coli* case. (right) The error bar of each individual point represents $\pm\sigma$ for $n = 5$.

resides in the human intestine. *E. coli* K12 is not a uropathogenic strain and is generally considered a non-pathogenic, commensal bacterium. We observed a significant response in the PANTOMIM biosensor for *E. coli* K12. This observation can be attributed to the surface proteins like adhesins, including outer membrane proteins and non-fimbrial proteins expressed by both *E. coli* strains (Wurpel et al., 2015). However, it is essential to note that while *E. coli* K12 and UPEC share some surface proteins, UPEC strains possess many unique virulence factors (i.e., hemolysin and P fimbriae) and genomic regions that are absent in *E. coli* K12, which likely play a more significant role in UPEC pathogenesis (Kaper et al., 2004).

In addition to the *E. coli* strains, *C. freundii,* a gram-negative rod-shaped bacterium found in the human intestinal flora, was examined. While *C. freundii* is a typical colonizer of healthy individuals, it can become pathogenic, causing infections in the urinary tract. While both *C. freundii* and UPEC are members of the Enterobacteriaceae family, they have distinct differences in their genetic diversity, phenotypic variations, and pathogenic behaviors (Liu et al., 2018). On the other hand, some studies reported structural similarity in the O-antigen epitopes (O-specific polysaccharides of their lipopolysaccharides, i.e., OCU158) of both pathogens, which was associated with the serological cross-reactivity observed between *C. freundii* and *E. coli* strains (Stenutz et al., 2006; Zhou et al., 2023). Fig. 4D examination showed no significant concentration-dependent change related to the presence of *C. freundii* on the surface. This suggests that *C. freundii*'s ability to adhere to surface substrates is limited, consistent with the SPR investigations that revealed a higher specificity for *UPEC* despite the cross-reactivity. *S. aureus*, a genus of gram-positive bacteria, naturally occurs in humans and animals and is a significant risk factor for uropathologic infections. It also showed no concentration-dependent significant binding response, as did *P. mirabilis*.

In repeatability studies of PANTOMIM biosensor arrays, the system was set up across ten distinct flow channels (Fig. S11), covering three different sensor regions, each functionalized as described previously. The study examined the surface binding properties of UPEC bacteria at a concentration of 10^2 cfu mL^{-1} over a 15-min period. To optimize the performance, the antibody layer was refreshed between measurements, with the same layer consistently proving effective for up to 2–3 detection cycles. Binding was observed in eight of the ten channels. These findings indicate successful outcomes in 80 % of the 30 sensor regions associated with UPEC.

3.5. PANTOMIM UPEC detection in clinical urine samples

Upon the promising biosensing performance of PANTOMIM in UPEC detection, we designed a clinical trial to assess the performance of PANTOMIM biosensors in clinical urine samples. We collected clinical urine samples from a cohort of 100 patients. For statistical analysis, we selected 50 UPEC+ and 50 UPEC− clinical samples. The UPEC− cohort consisted of 37 female and 13 male patients. Meanwhile, the UPEC + cohort consisted of 41 female and 9 male patients. All of these samples were tested in previously quality-checked PANTOMIM UPEC biosensors, each 3 replicates in independent microfluidic channels.

In Fig. 5A, we did a binary classification of resonance wavelength shift ($\Delta\lambda$) and normalized response for UPEC− and UPEC + clinical samples regardless of their clinically-detected UPEC concentration. The UPEC− clinical samples showed a mean $\Delta\lambda$ of 1.07 nm and a mean of 0.16 normalized response. On the other hand, the UPEC + clinical

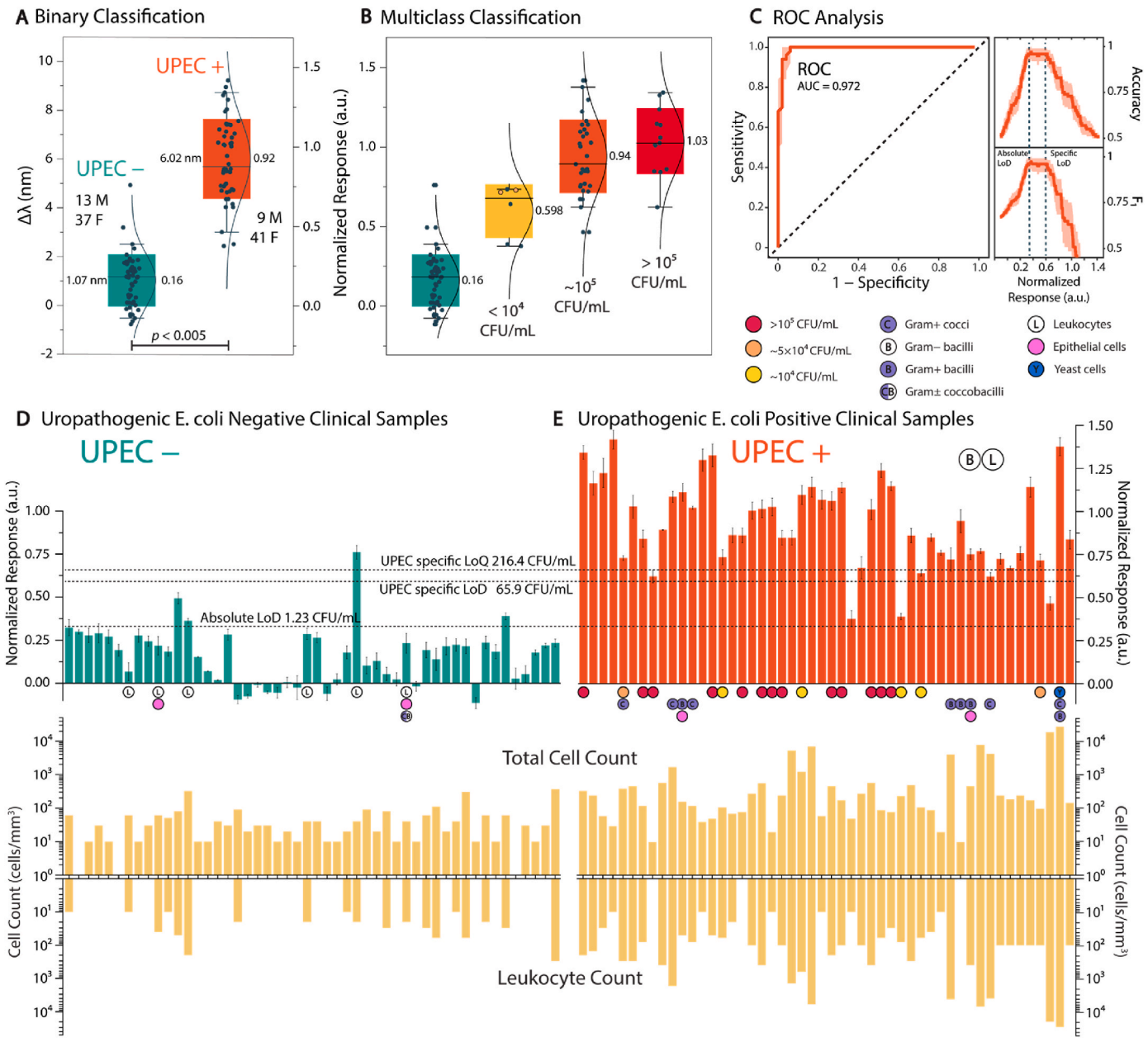

Fig. 5. **A** The binary classification of clinically tested uropathogenic *E. coli* (UPEC) negative and positive samples with respect to the plasmon resonance wavelength shift ($\Delta\lambda$). The clinical data set has a cohort of 100 individuals consisting of clinically diagnosed 50 UPEC+ and 50 UPEC−. The UPEC + cohort had 13 male and 37 female patients. The UPEC + cohort had 9 male and 41 female patients. The statistical significance ($p < 0.005$) was calculated using both Welch's *t*-test and Mann-Whitney *U* Test. **B** The multiclass classification of UPEC−, UPEC + results with a UPEC concentration of $<10^4$, $\sim10^5$, and $>10^5$ cfu mL^{-1} with respect to the normalized response of the PANTOMIM biosensor. The box chart height represents $\pm\sigma$ error bars, and the left-hand side curve represents the normal distribution. The values on the right and left side of the box chart represent the mean of the distribution with respect to resonance wavelength shift and normalized response, respectively. The horizontal line in the box chart represents the median of the statistical population. The box chart range repesents $\pm\sigma$. The whiskers represent 5 and 95 percentile. The normal distribution is presented on the right of the box chart. The mean value is represent on the right side as well. **C** The receiver operational characteristics (ROC) of PANTOMIM biosensor in binary classification of clinical samples. The accuracy and F1 predictive performance depend on the normalized response cut-offs. (right) The absolute and specific limit of detection (LoD) levels extracted from the in-vitro calibration curve are annotated in both figures. The shaded areas show 99 % and 95 % confidence intervals for ROC analysis and accuracy/F1 performance, respectively. **D** The normalized response of PANTOMIM biosensor for 50 clinically UPEC− samples. (top) The total cell and leukocyte counts from the clinical samples are presented in the log scale (bottom). **E** The normalized response of PANTOMIM biosensor for 50 clinically UPEC + samples. (top) The total cell and leukocyte counts from the clinical samples are presented in the log scale (bottom). The clinically detected UPEC levels for unannotated samples are 10^5 cfu mL^{-1}. The different levels are annotated using red, orange, and yellow circles for $>10^5$, $\sim5 \times 10^4$, and $<10^4$ cfu mL^{-1}, respectively. For all UPEC + samples, gram− bacilli and leukocytes were present in microscopic analysis. The presence of both species and interferants are annotated above section E.

samples had a mean $\Delta\lambda$ of 6.02 nm and a mean of 0.92 normalized response. The difference in the plasmonic response distribution was statistically significant ($p \ll 0.005$). The significant difference in response can also be attributed to the fact that the patient is diagnosed as UPEC + when the clinically detected UPEC level is greater than or equal to 10^4 cfu mL^{-1}.

The different levels of UPEC presence in urine samples were also proportional to the response in the PANTOMIM UPEC biosensor, as

shown in Fig. 5B. To set a response cut-off for UPEC diagnosis in the PANTOMIM UPEC biosensor, we used receiver operational characteristics (ROC) analysis. The ROC analysis showed that the area under the curve (AUC), which quantifies the specificity and sensitivity of a sensor, reaches a remarkable level of 0.972, as shown in Fig. 5C. Further analysis of the confusion matrix revealed that the accuracy and predictive performance (F_1) of the PANTOMIM UPEC biosensor reached over 90 %. When we delve deep into where accuracy and F1 values plateau, the lower response end coincides with the absolute limit of detection that we calculated earlier in spiked samples. We also defined a new parameter for the higher response end as the specific limit of detection where the response is much higher than the responses we get for non-specific bacteria such as *E. coli* K12, *C. freundii*, etc. This newly defined specific limit of detection value was around 65.9 cfu mL^{-1}. Using Equation (3) from earlier, we can also calculate the specific limit of quantification (10 σ condition) for our biosensor. For the PANTOMIM UPEC biosensor, the specific limit of quantification was determined as 216.4 cfu mL^{-1}, well below the value required (10^4 cfu mL^{-1}) for clinical diagnosis. We also considered other interferants, such as other types of bacteria or yeast cells or somatic cells like epithelial cells, or immune cells such as leukocytes, and labeled them in Fig. 5D, along with the total and white cell counts for each clinical sample. We used a syringe filter with a 5 μm mean pore size to eliminate large somatic cells to reduce the effects of such interferants. The PANTOMIM UPEC biosensor had only 1 false positive response, in which leukocytes were present in the clinical sample. Additional pre-filtration steps (such as consecutive filtering steps and/or cascading filtering using different pore sizes) could be implemented to ensure the removal of the human cells. However, the additional steps might also interfere with the large UPEC colonies present in the urine.

The clinical performance of the PANTOMIM UPEC biosensor was remarkable, considering that the measurement takes only 15 min from a small sample with minimal sample preparation (large cell filtration). We believe that PANTOMIM should be further tested in a larger clinical cohort to pave the way for its clinical deployment, cutting the UPEC diagnosis time from days to hours.

4. Conclusion

The development of the Plasmonic Array Nanohole Technology on Metal-Insulator-Metal (PANTOMIM) architecture represents a significant advancement in plasmonic biosensing technology. By addressing the limitations of conventional plasmonic nanohole arrays, PANTOMIM offers a robust platform for rapid and sensitive detection of uropathogenic Escherichia coli (UPEC) in clinical settings.The PANTOMIM design successfully incorporates the advantages of plasmonic nanohole arrays while mitigating the challenges associated with thin-film plasmonic metals. The metal-insulator-metal structure effectively dampens metal/substrate peaks, ensuring high extinction coefficients and spectral purity, which are crucial for biosensing applications. The optimization of the architecture for the 800–850 nm wavelength range aligns well with the quantum efficiency profile of low-cost Si-based sensors, paving the way for future integration into nanophotonic devices.Our experimental results demonstrate the high performance of the PANTOMIM sensors in terms of spectral response, RI sensitivity, and reproducibility. The close agreement between the simulated and experimental data validates the design principles and fabrication methods used. Successful detection of UPEC in urine samples in 15 min, with minimal sample preparation, showcases the potential of the technology to revolutionize urinary tract infection diagnostics. Clinical validation of PANTOMIM UPEC biosensors with a cohort of 100 patients underscores its readiness for real-world applications. This rapid detection method offers a significant improvement over traditional culture-based techniques, which could lead to a faster diagnosis and treatment of urinary tract infections. Looking ahead, the PANTOMIM platform holds promise for broader applications in point of care diagnostics. Its high sensitivity, spectral purity, and compatibility with existing optical components make it an attractive option for detecting various biomarkers and pathogens. Future research should focus on expanding the range of detectable analytes and further miniaturizing the system for portable diagnostic devices.In conclusion, PANTOMIM represents a bridge between laboratory innovation and clinical application in biosensing technology. By combining advanced nanofabrication techniques with clever optical design, we have created a powerful tool for the rapid, sensitive, and specific detection of pathogens. As we continue to refine and expand this technology, PANTOMIM has the potential to significantly impact the field of medical diagnostics, offering faster, more accurate and more accessible testing options for a wide range of health conditions.

CRediT authorship contribution statement

Hasan Kurt: Writing – review & editing, Writing – original draft, Visualization, Validation, Supervision, Resources, Project administration, Methodology, Funding acquisition, Formal analysis, Data curation, Conceptualization. **Caner Soylukan:** Writing – original draft, Validation, Investigation, Data curation. **Süleyman Çelik:** Resources, Methodology, Investigation. **Eda Çapkın:** Resources, Methodology, Investigation, Formal analysis. **Ibrahim Cagatay Acuner:** Funding acquisition, Conceptualization. **Aynur Eren Topkaya:** Validation, Resources, Investigation. **Meral Yüce:** Writing – review & editing, Supervision, Project administration, Funding acquisition, Conceptualization.

Data and materials availability

All processed data are available in the main text or the supplementary materials. The unprocessed data that support the findings of this study are available from the corresponding author upon reasonable request.

Declaration of competing interest

The authors declare the following financial interests/personal relationships which may be considered as potential competing interests: Meral Yuce reports financial support was provided by Scientific and Technological Research Council of Turkey. Hasan Kurt reports financial support was provided by UK Research and Innovation. Hasan Kurt has patent #WO2023191739A1 pending to Sabanci University Nanotechnology Research and Application Center. If there are other authors, they declare that they have no known competing financial interests or personal relationships that could have appeared to influence the work reported in this paper.

Acknowledgement

The authors thank The Scientific and Technological Research Council of Turkey, 1004 Center of Excellence Support Program Grant ID: 20AG011, for financial support. HK acknowledges the EU Horizon Europe Marie Skłodowska-Curie fellowship (Ref: 101111321) and UKRI MSCA fellowship (EP/Y030273/1) for their support. We would also like to thank Zeki Semih Pehlivan for training the students and staff on the initial fabrication steps, Sumeyra Vural Kaymaz for the technical assistance in microfluidic fabrication, and Begum Balkan Apaydin for initial buffer optimizations.

Appendix A. Supplementary data

Supplementary data to this article can be found online at https://doi.org/10.1016/j.bios.2025.117419.

Data availability

Data will be made available on request.

References

Aydin, K., Ferry, V.E., Briggs, R.M., Atwater, H.A., 2011. Broadband polarization-independent resonant light absorption using ultrathin plasmonic super absorbers. Nat. Commun. 2, 517. https://doi.org/10.1038/ncomms1528.

Belushkin, A., Yesilkoy, F., González-López, J.J., Ruiz-Rodríguez, J.C., Ferrer, R., Fàbrega, A., Altug, H., 2020. Rapid and digital detection of inflammatory biomarkers enabled by a novel portable nanoplasmonic imager. Small 16, 1906108. https://doi.org/10.1002/smll.201906108.

Cetin, A.E., 2024. A portable plasmonic biosensor kit for diagnostics of sexually transmitted infection. Plasmonics 19, 753–764. https://doi.org/10.1007/s11468-023-02035-0.

Cetin, A.E., Etezadi, D., Galarreta, B.C., Busson, M.P., Eksioglu, Y., Altug, H., 2015. Plasmonic nanohole arrays on a robust hybrid substrate for highly sensitive label-free biosensing. ACS Photonics 2, 1167–1174. https://doi.org/10.1021/acsphotonics.5b00242.

Chanda, D., Shigeta, K., Truong, T., Lui, E., Mihi, A., Schulmerich, M., Braun, P.V., Bhargava, R., Rogers, J.A., 2011. Coupling of plasmonic and optical cavity modes in quasi-three-dimensional plasmonic crystals. Nat. Commun. 2, 479. https://doi.org/10.1038/ncomms1487.

Flores-Mireles, A.L., Walker, J.N., Caparon, M., Hultgren, S.J., 2015. Urinary tract infections: epidemiology, mechanisms of infection and treatment options. Nat. Rev. Microbiol. 13, 269–284. https://doi.org/10.1038/nrmicro3432.

Gomez-Cruz, J., Nair, S., Manjarrez-Hernandez, A., Gavilanes-Parra, S., Ascanio, G., Escobedo, C., 2018. Cost-effective flow-through nanohole array-based biosensing platform for the label-free detection of uropathogenic E. coli in real time. Biosens. Bioelectron. 106, 105–110. https://doi.org/10.1016/J.BIOS.2018.01.055.

Kaper, J.B., Nataro, J.P., Mobley, H.L.T., 2004. Pathogenic Escherichia coli. Nat. Rev. Microbiol. 2 (2 2), 123–140. https://doi.org/10.1038/nrmicro818, 2004.

Kaymaz, S.V., Nobar, H.M., Sarıgül, H., Soylukan, C., Akyüz, L., Yüce, M., 2023. Nanomaterial surface modification toolkit: principles, components, recipes, and applications. Adv. Colloid Interface Sci. 322, 103035. https://doi.org/10.1016/J.CIS.2023.103035.

Kurt, H., Pishva, P., Pehlivan, Z.S., Arsoy, E.G., Saleem, Q., Bayazıt, M.K., Yüce, M., 2021. Nanoplasmonic biosensors: theory, structure, design, and review of recent applications. Anal. Chim. Acta 1185, 338842. https://doi.org/10.1016/J.ACA.2021.338842.

Lecarme, O., Sun, Q., Ueno, K., Misawa, H., 2014. Robust and versatile light absorption at near-infrared wavelengths by plasmonic aluminum nanorods. ACS Photonics 1, 538–546. https://doi.org/10.1021/ph500096q.

Li, X., Soler, M., Özdemir, C.I., Belushkin, A., Yesilköy, F., Altug, H., 2017. Plasmonic nanohole array biosensor for label-free and real-time analysis of live cell secretion. Lab Chip 17, 2208–2217. https://doi.org/10.1039/C7LC00277G.

Liu, Liyun, Chen, D., Liu, Liqin, Lan, R., Hao, S., Jin, W., Sun, H., Wang, Y., Liang, Y., Xu, J., 2018. Genetic diversity, multidrug resistance, and virulence of citrobacter freundii from diarrheal patients and healthy individuals. Front. Cell. Infect. Microbiol. 8, 384577. https://doi.org/10.3389/FCIMB.2018.00233/BIBTEX.

Müller, K.M., Arndt, K.M., Plückthun, A., 1998. Model and simulation of multivalent binding to fixed ligands. Anal. Biochem. 261, 149–158. https://doi.org/10.1006/abio.1998.2725.

Nair, S., Gomez-Cruz, J., Manjarrez-Hernandez, Á., Ascanio, G., Sabat, R.G., Escobedo, C., 2020. Rapid label-free detection of intact pathogenic bacteria *in situ via* surface plasmon resonance imaging enabled by crossed surface relief gratings. Analyst 145, 2133–2142. https://doi.org/10.1039/C9AN02339A.

Nair, S., Gomez-Cruz, J., Manjarrez-Hernandez, Á., Ascanio, G., Sabat, R.G., Escobedo, C., 2018. Selective uropathogenic E. coli detection using crossed surface-relief gratings. Sensors 18, 3634. https://doi.org/10.3390/s18113634.

Rowe, T.A., Juthani-Mehta, M., 2014. Diagnosis and management of urinary tract infection in older adults. Infect. Dis. Clin. 28, 75–89. https://doi.org/10.1016/j.idc.2013.10.004.

Soler, M., Belushkin, A., Cavallini, A., Kebbi-Beghdadi, C., Greub, G., Altug, H., 2017. Multiplexed nanoplasmonic biosensor for one-step simultaneous detection of Chlamydia trachomatis and Neisseria gonorrhoeae in urine. Biosens. Bioelectron. 94, 560–567. https://doi.org/10.1016/j.bios.2017.03.047.

Steen Redeker, E., Ta, D.T., Cortens, D., Billen, B., Guedens, W., Adriaensens, P., 2013. Protein engineering for directed immobilization. Bioconjug. Chem. 24, 1761–1777. https://doi.org/10.1021/bc4002823.

Stenutz, R., Weintraub, A., Widmalm, G., 2006. The structures of Escherichia coli O-polysaccharide antigens. FEMS Microbiol. Rev. 30, 382–403. https://doi.org/10.1111/J.1574-6976.2006.00016.X.

Wurpel, D.J., Moriel, D.G., Totsika, M., Easton, D.M., Schembri, M.A., 2015. Comparative analysis of the uropathogenic Escherichia coli surface proteome by tandem mass-spectrometry of artificially induced outer membrane vesicles. J. Proteonomics 115, 93–106. https://doi.org/10.1016/J.JPROT.2014.12.005.

Yanik, A.A., Cetin, A.E., Huang, M., Artar, A., Mousavi, S.H., Khanikaev, A., Connor, J.H., Shvets, G., Altug, H., 2011a. Seeing protein monolayers with naked eye through plasmonic Fano resonances. Proc. Natl. Acad. Sci. U. S. A. 108, 11784–11789. https://doi.org/10.1073/pnas.1101910108.

Yanik, A.A., Cetin, A.E., Huang, M., Artar, A., Mousavi, S.H., Khanikaev, A., Connor, J.H., Shvets, G., Altug, H., 2011b. Seeing protein monolayers with naked eye through plasmonic Fano resonances. Proc. Natl. Acad. Sci. USA 108, 11784–11789. https://doi.org/10.1073/pnas.1101910108.

Yanik, A.A., Huang, M., Kamohara, O., Artar, A., Geisbert, T.W., Connor, J.H., Altug, H., 2010. An optofluidic nanoplasmonic biosensor for direct detection of live viruses from biological media. Nano Lett. 10, 4962–4969. https://doi.org/10.1021/nl103025u.

Yüce, M., Kurt, H., 2017. How to make nanobiosensors: surface modification and characterisation of nanomaterials for biosensing applications. RSC Adv. 7, 49386–49403. https://doi.org/10.1039/c7ra10479k.

Zhou, Y., Zhou, Z., Zheng, L., Gong, Z., Li, Y., Jin, Y., Huang, Y., Chi, M., 2023. Urinary tract infections caused by uropathogenic Escherichia coli: mechanisms of infection and treatment options. Int. J. Mol. Sci. 24, 10537. https://doi.org/10.3390/IJMS241310537.